



HAL
open science

Optimal Experimental Design for the Assessment of Thermophysical Properties in Existing Building Walls

Suelen Gasparin, Julien Berger, Giampaolo D'alessandro, Filippo de Monte,
Dariusz Ucinski

► **To cite this version:**

Suelen Gasparin, Julien Berger, Giampaolo D'alessandro, Filippo de Monte, Dariusz Ucinski. Optimal Experimental Design for the Assessment of Thermophysical Properties in Existing Building Walls. Heat Transfer Engineering, 2023, 10.1080/01457632.2023.2241176 . hal-04297881v2

HAL Id: hal-04297881

<https://hal.science/hal-04297881v2>

Submitted on 24 Nov 2023

HAL is a multi-disciplinary open access archive for the deposit and dissemination of scientific research documents, whether they are published or not. The documents may come from teaching and research institutions in France or abroad, or from public or private research centers.

L'archive ouverte pluridisciplinaire **HAL**, est destinée au dépôt et à la diffusion de documents scientifiques de niveau recherche, publiés ou non, émanant des établissements d'enseignement et de recherche français ou étrangers, des laboratoires publics ou privés.



Distributed under a Creative Commons Attribution - NonCommercial - NoDerivatives 4.0 International License

Optimal experimental design for the assessment of thermophysical properties in existing building walls

Suelen Gasparin^{a,b}, Julien Berger^c, Giampaolo D'Alessandro^d, Filippo de Monte^d and

Dariusz Ucinski^e

^a Cerema, French Ministry of Ecological Transition, BPE Research team, 44200 Nantes, France

^b Univ. Savoie Mont Blanc, UMR 5271 CNRS, LOCIE, 73000 Chambéry, France

^c Laboratory of Engineering Sciences for the Environment (LaSIE), UMR 7356 CNRS, La Rochelle University, CNRS, 17000, La Rochelle, France

^d Department of Industrial and Information Engineering and Economics, University of L'Aquila, 67100 L'Aquila, Italy

^e Institute of Control and Computation Engineering, University of Zielona Góra, ul. Szafrana 2, 65-516 Zielona Góra, Poland

Abstract

The estimation of wall thermal properties through an inverse problem procedure enables to increase the reliability of the model predictions for building energy efficiency. Nevertheless, it requires defining an experimental campaign to obtain *in situ* observations for existing buildings. The quality of the estimated parameter strongly depends on the quality of the experimental data used for the parameter identification. In other words, there is a close relation between the experiment design and the precision of the retrieved parameters. The design of experiments enables to search for the optimal measurement plan. It ensures the highest precision of the parameter to be estimated. For *in situ* measurement in buildings, the design of experiments seeks to answer the following questions: How many sensors do we need? What is the sensor position in the wall? The optimal experiment design methodology enables us to answer those questions. The unknown parameter is the thermal conductivity of wall façade modeled considering two-dimensional heat transfer induced by time and space varying boundary conditions.

CONTACT: Dr. Suelen Gasparin, French Ministry of Ecological Transition, Cerema, BPE
Research team, 44200 Nantes, France. E-mail: suelen.gasparin@cerema.fr

Introduction

In Europe, approximately 80% of today's buildings will still be in use in 2050, in which 75% of this stock is energy inefficient, highlighting a crucial environmental issue on building retrofiting. To efficiently plan such actions, *in-situ* diagnoses are required to determine the uncertain thermophysical properties of the materials composing the walls. This kind of problem can be solved using experimental observations of the temperature inside the wall [1] and solving inverse problem [2]. To maximize the accuracy of the estimation, the optimal experiment design (OED) can be carried out before the *in-situ* experiments so the parameters to be estimated have minimum variance. There is a close relation between the experiment design and the precision of the retrieved parameters [3]. For example, Nenamorokov et al. [4] searched the OED for the estimation of radiation properties while in [5] and [6] the OED is defined for the estimation of thermal properties of high conductivity materials. Artyukhin and Budnik [7] inspected the optimal sensor location and their quantity in the inverse heat conduction boundary problem. More recently, in [8], the optimal heating period and the duration of the experiment were investigated for the thermal conductivity estimation in building walls. In this article, the OED is explored concerning the sensor positioning, considering a two-dimensional inverse heat conduction problem [9] in a wall façade composed of concrete and subjected to climatic boundary conditions. The latter are varying according to time and space. The OED is determined by solving an optimization problem. It seeks in determining the decision elements to place a sensor at one position (0/1 sensor). Since the exhaustive search is too expensive in terms of computational cost, two alternative strategies are investigated. The first one uses an exchange algorithm which ensure to find a local optimal solution. With the second strategy, the problem is relaxed by setting the decision elements as real numbers in unit interval. Thus, probabilities of sensor positioning are obtained and convergence of algorithm is faster. The article is structured as follows. First, the mathematical model is described. Then, the numerical model to solve the governing equation is presented and verified using an analytical solution. Section introduces the D-optimum criterion and optimization strategies

to determine the OED. A realistic case study is then considered in Section before addressing some conclusion and outlooks for future works.

Mathematical formulation of the problem

The transfer problem considers heat conduction through a solid material as illustrated in Figure 1 and described by the following partial differential equation:

$$\rho c_p \frac{\partial T}{\partial t} = \nabla \cdot (\lambda \nabla T) \quad (1)$$

where ρ [$\text{kg} \cdot \text{m}^{-3}$], the material density, c_p [$\text{J} \cdot \text{kg}^{-1} \cdot \text{K}^{-1}$] is the material specific heat, T [K] is the temperature, t [s] is the time, and λ [$\text{W} \cdot \text{m}^{-1} \cdot \text{K}^{-1}$] being the thermal conductivity. The transport phenomena is observed for the duration $t \in [0, \tau]$, where τ [s] is the horizon time of simulation. For two-dimensional transfers, the spatial domain is defined for $x \in [0, l_x]$ and $y \in [0, l_y]$ with l_x [m] and l_y [m] being the thickness and the height of the material.

At boundaries a mixed-type condition is defined, which include the convection and short-wave length radiation phenomena:

$$\lambda \frac{\partial T}{\partial x} = h^L(y, t) \left(T - T_\infty^L(t) \right) - \alpha q_\infty(y, t), \quad \text{for } x = 0, \quad \forall y, \quad t > 0 \quad (2a)$$

$$-\lambda \frac{\partial T}{\partial x} = h^R \left(T - T_\infty^R(t) \right), \quad \text{for } x = l_x, \quad \forall y, \quad t > 0 \quad (2b)$$

$$-\lambda \frac{\partial T}{\partial y} = h^T \left(T - T_\infty^T(t) \right), \quad \text{for } y = l_y, \quad \forall x, \quad t > 0 \quad (2c)$$

$$\lambda \frac{\partial T}{\partial y} = h^B \left(T - T_\infty^B(t) \right), \quad \text{for } y = 0, \quad \forall x, \quad t > 0 \quad (2d)$$

where T_∞ [K] is the ambient air temperature and h [$\text{W} \cdot \text{m}^{-2} \cdot \text{K}^{-1}$] is the convective heat transfer coefficient. In the bounding surface in contact with the outdoor air, q_∞ [$\text{W} \cdot \text{m}^{-2}$] is the total solar radiation, which includes the direct, diffuse and reflexive radiations and α is the surface solar absorptivity. The solar absorptivity is assumed as a known constant since the

wall is considered as a diffuse-gray surface [10].

For the initial condition, at $t = 0$, a two-dimensional temperature distribution in function of space is considered:

$$T(x, y, 0) = T_0(x, y) \quad (3)$$

Dimensionless form

It is of capital importance to get a dimensionless formulation of the problem under consideration before solving the problem directly. Important scaling parameters are defined so that a whole class of dimensional problems can be solved. It may also allow to simplify the problem based on asymptotic methods. Last, the rounding errors are minimal if computer manipulates numbers of same magnitude. In this way, the following dimensionless quantities for one dimensional transfer are defined:

$$\begin{aligned} u & \stackrel{\text{def}}{:=} \frac{T - T_{\text{ref}}}{\Delta T_{\text{ref}}}, & x^* & \stackrel{\text{def}}{:=} \frac{x}{l_x}, & y^* & \stackrel{\text{def}}{:=} \frac{y}{l_y}, & t^* & \stackrel{\text{def}}{:=} \frac{t}{t_{\text{ref}}}, & \nu & \stackrel{\text{def}}{:=} \frac{t_{\text{ref}} \cdot \lambda}{l_x^2 \cdot \rho \cdot c_p}, \\ R & \stackrel{\text{def}}{:=} \frac{l_x^2}{l_y^2}, & \text{Bi}^L & \stackrel{\text{def}}{:=} \frac{h^L \cdot l_x}{\lambda}, & \text{Bi}^R & \stackrel{\text{def}}{:=} \frac{h^R \cdot l_x}{\lambda}, & \text{Bi}^T & \stackrel{\text{def}}{:=} \frac{h^T \cdot l_y}{\lambda}, & \text{Bi}^B & \stackrel{\text{def}}{:=} \frac{h^B \cdot l_y}{\lambda}, \\ q_\infty^* & \stackrel{\text{def}}{:=} \frac{l_x \cdot \alpha \cdot q_\infty}{\Delta T_{\text{ref}} \cdot \lambda} \end{aligned} \quad (4)$$

where the subscript ref represents a reference value, chosen according to the application problem and the star \star represents a dimensionless quantity of the same parameter. Therefore, the governing Equation (1), for two dimensional transfer can be written in a dimensionless form as:

$$\frac{\partial u}{\partial t^*} = \nu \frac{\partial^2 u}{\partial x^{*\ 2}} + \nu R \frac{\partial^2 u}{\partial y^{*\ 2}} \quad (5)$$

The dimensionless formulation of the boundary conditions are:

$$\left. \frac{\partial u}{\partial x^*} \right|_{x^*=0} = \text{Bi}^L \left(u - u_{\infty}^L(t^*) \right) - q_{\infty}^*(y^*, t^*) \quad (6a)$$

$$-\left. \frac{\partial u}{\partial x^*} \right|_{x^*=1} = \text{Bi}^R \left(u - u_{\infty}^R(t^*) \right) \quad (6b)$$

$$-\left. \frac{\partial u}{\partial y^*} \right|_{y^*=1} = \text{Bi}^T \left(u - u_{\infty}^T(t^*) \right) \quad (6c)$$

$$\left. \frac{\partial u}{\partial y^*} \right|_{y^*=0} = \text{Bi}^B \left(u - u_{\infty}^B(t^*) \right) \quad (6d)$$

and the initial condition:

$$u(x^*, y^*, 0) = u_0(x^*, y^*) \quad (7)$$

Numerical solution for the direct problem

The 2D-Spectral-ROM method

Consider the linear isotropic diffusion Equation (5) for the two-dimensional space transformed to the canonical interval $\bar{x}, \bar{y} \in [-1, 1]$. By using the Spectral-ROM approach, the solution is approximated by the sum [11]:

$$u(\bar{x}, \bar{y}, t^*) \approx \sum_{i=1}^N \sum_{j=1}^M a_{ij}(t^*) \mathbb{T}_{i-1}(\bar{x}) \mathbb{T}_{j-1}(\bar{y}) \quad (8)$$

Here, $\{\mathbb{T}_{i-1}(\bar{x})\}_{i=1}^N$ and $\{\mathbb{T}_{j-1}(\bar{y})\}_{j=1}^M$ are sets of basis functions (Chebyshev polynomials) and $\{a_{ij}(t)\}_{i,j=1}^{N,M}$ are the corresponding time-dependent spectral coefficients which are the unknowns of the problem. This approach is proven to be very efficient in one dimensional problems

[12]. Then, the residual \mathcal{R} is composed by substituting Equation (8) into Equation (5):

$$\begin{aligned} \mathcal{R}(\bar{x}, \bar{y}, t^*) &= \sum_{i=1}^N \sum_{j=1}^M \dot{a}_{ij}(t^*) \mathsf{T}_{i-1}(\bar{x}) \mathsf{T}_{j-1}(\bar{y}) - 4\nu \sum_{i=1}^N \sum_{j=1}^M \tilde{a}_{ij}^x(t^*) \mathsf{T}_{i-1}(\bar{x}) \mathsf{T}_{j-1}(\bar{y}) \\ &\quad - 4\nu \mathsf{R} \sum_{i=1}^N \sum_{j=1}^M \tilde{a}_{ij}^y(t^*) \mathsf{T}_{i-1}(\bar{x}) \mathsf{T}_{j-1}(\bar{y}) \end{aligned} \quad (9)$$

where $\dot{a}_{ij} \stackrel{\text{def}}{=} \frac{da_{ij}(t^*)}{dt^*}$. The spatial derivatives are expanded in the same Chebyshev basis function. Thus, coefficients \tilde{a}_{ij}^x and \tilde{a}_{ij}^y are expressed in terms of coefficients a_{ij} according to the explicit relations obtained from the recurrence relation of the Chebyshev polynomial derivatives [13]. Here, \tilde{a}_{ij}^x and \tilde{a}_{ij}^y denotes:

$$\tilde{a}_{ij}^x = \frac{1}{c_i} \sum_{\substack{p=i+2 \\ p+i \text{ even}}}^N p(p^2 - i^2) a_{pj}, \quad i \in \{1, 2, \dots, N-2\} \quad (10a)$$

$$\tilde{a}_{N-1j}^x \equiv \tilde{a}_{Nj}^x \equiv 0, \quad \forall j \in \{1, 2, \dots, M\} \quad (10b)$$

$$\tilde{a}_{ij}^y = \frac{1}{c_j} \sum_{\substack{p=j+2 \\ p+j \text{ even}}}^M p(p^2 - j^2) a_{ip}, \quad j \in \{1, 2, \dots, M-2\} \quad (10c)$$

$$\tilde{a}_{iM-1}^y \equiv \tilde{a}_{iM}^y \equiv 0, \quad \forall i \in \{1, 2, \dots, N\} \quad (10d)$$

with the constants c_i and c_j being given by:

$$c_k = \begin{cases} 2, & k = 0 \\ 1, & k > 0 \end{cases} \quad (11)$$

The residual $\mathcal{R}(\bar{x}, \bar{y}, t^*)$ is minimized via the collocation method:

$$\mathcal{R}(\bar{x}_k, \bar{y}_l, t^*) = 0 \quad (12)$$

which requires that the residual be equal to zero at the Chebyshev–Gauss–Lobatto points:

$$\bar{x}_k = -\cos\left(\frac{\pi \cdot k}{N-1}\right), \quad k \in \{0, 1, 2, \dots, N-1\} \quad (13a)$$

$$\bar{y}_l = -\cos\left(\frac{\pi \cdot l}{M-1}\right), \quad l \in \{0, 1, 2, \dots, M-1\} \quad (13b)$$

These points are chosen in order to minimize the error of the numerical solution and to avoid Runge’s phenomenon [14]. Figure 2 presents the spatial distribution of the points following Equation (13).

To solve the problem, the residual can be written in a matricial form. For this, consider the spatial derivatives approximated as in [15]:

$$\begin{aligned} \frac{\partial^2 u}{\partial \bar{x}^2} &= \sum_{i=1}^N \sum_{j=1}^M \Upsilon_{i-1}(\bar{x}_k) \Upsilon_{j-1}(\bar{y}_l) \tilde{a}_{ij}^x(t^*) \\ &= [C(\bar{x}_k) \otimes C(\bar{y}_l)] \cdot [(\tilde{D}_x \otimes \mathbf{Id}_y) \cdot A_{ij}(t^*)] \end{aligned} \quad (14)$$

and

$$\begin{aligned} \frac{\partial^2 u}{\partial \bar{y}^2} &= \sum_{i=1}^N \sum_{j=1}^M \Upsilon_{i-1}(\bar{x}_k) \Upsilon_{j-1}(\bar{y}_l) \tilde{a}_{ij}^y(t^*) \\ &= [C(\bar{x}_k) \otimes C(\bar{y}_l)] \cdot [(\mathbf{Id}_x \otimes \tilde{D}_y) \cdot A_{ij}(t^*)] \end{aligned} \quad (15)$$

where \mathbf{Id}_x is the identity matrix of size $N \times N$ with respect to \bar{x} , \mathbf{Id}_y is the identity matrix of size $M \times M$ with respect to \bar{y} and the operation denoted by \otimes is the Kronecker product [16].

The matrix of spectral coefficients $\{a_{ij}\}_{i,j=1}^{N,M}$ was transformed into a vector:

$$A_{ij} = [a_{11}, a_{12}, \dots, a_{1N}, a_{21}, a_{22}, \dots, a_{2N}, a_{M1}, a_{M2}, \dots, a_{MN}]_{(NM \times 1)}^\top \quad (16)$$

In addition, \tilde{D}_x and \tilde{D}_y correspond to the second order differentiation matrices with respect to x and y respectively such that $\tilde{D}_x \in \text{Mat}_{N \times N}(\mathbb{R})$ and $\tilde{D}_y \in \text{Mat}_{M \times M}(\mathbb{R})$, which are deduced

from the recurrence relation [17, Eq.3.26]. Finally, the vector of the Chebyshev polynomial values are:

$$C(\bar{x}_k) = [\mathbb{T}_0(\bar{x}_k), \mathbb{T}_1(\bar{x}_k), \mathbb{T}_2(\bar{x}_k), \dots, \mathbb{T}_N(\bar{x}_k)]_{(1 \times N)} \quad (17a)$$

$$C(\bar{y}_l) = [\mathbb{T}_0(\bar{y}_l), \mathbb{T}_1(\bar{y}_l), \mathbb{T}_2(\bar{y}_l), \dots, \mathbb{T}_M(\bar{y}_l)]_{(1 \times M)} \quad (17b)$$

Therefore, the original problem is reduced to a system of ordinary differential equations, which has the following form:

$$[C(\bar{x}_k) \otimes C(\bar{y}_l)] \cdot \dot{A}_{ij} = [C(\bar{x}_k) \otimes C(\bar{y}_l)] \cdot [(4\nu R \cdot \mathbf{Id}_x \otimes \tilde{\tilde{D}}_y + 4\nu \cdot \tilde{\tilde{D}}_x \otimes \mathbf{Id}_y) \cdot A_{ij}] \quad (18)$$

which is valid only for the internal collocation points:

$$k = 1, 2, \dots, N - 2 \quad \text{and} \quad l = 1, 2, \dots, M - 2.$$

The approximation of the solution and derivatives are also applied to the four boundary con-

ditions equations which complete the problem:

$$-\sum_{i=1}^N \sum_{j=1}^M \tilde{a}_{ij}^x(t^*) \mathbb{T}_{i-1}(-1) \mathbb{T}_{j-1}(\bar{y}_l) + \frac{\text{Bi}^L}{2} \left[\sum_{i=1}^N \sum_{j=1}^M a_{ij}(t^*) \mathbb{T}_{i-1}(-1) \mathbb{T}_{j-1}(\bar{y}_l) - u_{\infty}^L(t^*) \right] - \frac{q_{\infty}^*(t^*)}{2} = 0 \quad (19a)$$

$$\sum_{i=1}^N \sum_{j=1}^M \tilde{a}_{ij}^x(t^*) \mathbb{T}_{i-1}(1) \mathbb{T}_{j-1}(\bar{y}_l) + \frac{\text{Bi}^R}{2} \left[\sum_{i=1}^N \sum_{j=1}^M a_{ij}(t^*) \mathbb{T}_{i-1}(1) \mathbb{T}_{j-1}(\bar{y}_l) - u_{\infty}^L(t^*) \right] = 0 \quad (19b)$$

$$-\sum_{i=1}^N \sum_{j=1}^M \tilde{a}_{ij}^y(t^*) \mathbb{T}_{i-1}(\bar{x}_k) \mathbb{T}_{j-1}(-1) + \frac{\text{Bi}^B}{2} \left[\sum_{i=1}^N \sum_{j=1}^M a_{ij}(t^*) \mathbb{T}_{i-1}(\bar{x}_k) \mathbb{T}_{j-1}(-1) - u_{\infty}^B(t^*) \right] = 0 \quad (19c)$$

$$\sum_{i=1}^N \sum_{j=1}^M \tilde{a}_{ij}^y(t^*) \mathbb{T}_{i-1}(\bar{x}_k) \mathbb{T}_{j-1}(1) + \frac{\text{Bi}^T}{2} \left[\sum_{i=1}^N \sum_{j=1}^M a_{ij}(t^*) \mathbb{T}_{i-1}(\bar{x}_k) \mathbb{T}_{j-1}(1) - u_{\infty}^T(t^*) \right] = 0 \quad (19d)$$

Again, the coefficients \tilde{a}_{ij}^x and \tilde{a}_{ij}^y are deduced explicitly from the recurrence relation of the polynomials:

$$\tilde{a}_{ij}^x = \frac{2}{c_i} \sum_{\substack{p=i+1 \\ p+i \text{ odd}}}^N p a_{pj}, \quad i \in \{1, 2, \dots, N-1\}, \quad (20a)$$

$$\tilde{a}_{Nj}^x \equiv 0, \quad \forall j \in \{1, 2, \dots, M\}, \quad (20b)$$

$$\tilde{a}_{ij}^y = \frac{2}{c_j} \sum_{\substack{p=j+1 \\ p+j \text{ odd}}}^M p a_{ip}, \quad j \in \{1, 2, \dots, M-1\}, \quad (20c)$$

$$\tilde{a}_{iM}^y \equiv 0, \quad \forall i \in \{1, 2, \dots, N\}, \quad (20d)$$

Equation (19) has the following matrix compact form:

$$- [C(-1) \otimes C(\bar{y}_l)] \cdot [(\tilde{D}_x \otimes \mathbf{Id}_y) \cdot A_{ij}] + \frac{\text{Bi}^L}{2} [C(-1) \otimes C(\bar{y}_l) \cdot A_{ij} - u_\infty^L(t^*)] - \frac{q_\infty^*(t^*)}{2} = 0 \quad (21a)$$

$$[C(1) \otimes C(\bar{y}_l)] \cdot [(\tilde{D}_x \otimes \mathbf{Id}_y) \cdot A_{ij}] + \frac{\text{Bi}^R}{2} [C(1) \otimes C(\bar{y}_l) \cdot A_{ij} - u_\infty^R(t^*)] = 0 \quad (21b)$$

$$- [C(\bar{x}_k) \otimes C(-1)] \cdot [(\mathbf{Id}_x \otimes \tilde{D}_y) \cdot A_{ij}] + \frac{\text{Bi}^B}{2} [C(\bar{x}_k) \otimes C(-1) \cdot A_{ij} - u_\infty^B(t^*)] = 0 \quad (21c)$$

$$[C(\bar{x}_k) \otimes C(1)] \cdot [(\mathbf{Id}_x \otimes \tilde{D}_y) \cdot A_{ij}] + \frac{\text{Bi}^T}{2} [C(\bar{x}_k) \otimes C(1) \cdot A_{ij} - u_\infty^T(t^*)] = 0 \quad (21d)$$

where \tilde{D}_y corresponds to the first order differentiation matrix with respect to y , such that $\tilde{D}_y \in \text{Mat}(M \times M)$, which is deduced from the recurrence relation [17, Eq.3.23].

Initial values of the coefficients $\{a_{ij}(t = 0)\} \stackrel{\text{def}}{=} b_{ij}$ are calculated by approximating the initial condition $u_0(\bar{x}, \bar{y})$ as:

$$u_0(\bar{x}, \bar{y}) = \sum_{i=1}^N \sum_{j=1}^M b_{ij} \mathbb{T}_{i-1}(\bar{x}) \mathbb{T}_{j-1}(\bar{y}) \quad (22)$$

which is expanded and solved for b_{ij} using the collocation points.

Therefore, the time-dependent coefficients $\{a_{ij}\}_{i,j=1}^{N,M}$ are computed by solving the following system of ordinary differential equations:

$$\begin{cases} \mathcal{M} \cdot \dot{a}_{ij} &= f(t, a_{ij}) \\ a_{ij}(0) &= b_{ij} \end{cases} \quad (23)$$

where, $\mathcal{M} \in \text{Mat}_{NM \times NM}(\mathbb{R})$ is the mass matrix and $f(t, a_{ij}) \in \mathbb{R}^{NM}$ is a vector. To solve the System (23), the technique described in [18, Chap. 10] is employed. The matrix \mathcal{M} and the vector $f(t, a_{ij})$ are composed by the lines of the grid. Algorithm in Table 1 describes the process to compose $f(t, a_{ij})$ which is similar to \mathcal{M} . The integration in time is performed with

the use of the solver ode15s as in the previous spectral applications.

Verification of 2D-Spectral-ROM solution

Numerical solution are today verified considering analytical solution according to ASME [19] and following the method of exact solution [20]. For this reason the numerical solution proposed in previous section will be verified using an analytical solution for a two-dimensional transient phenomenon discussed in [21]. Since it is always difficult to obtain analytical solution for complex and realistic cases, a comparison test is carried with another numerical method in appendix.

Metrics

To analyze the accuracy of the method, the error between the simulated solution u^{num} , and the reference solution u^{ref} , are computed as functions of x^* and y^* using the following Euclidean norm:

$$\varepsilon_2(x^*, y^*) \stackrel{\text{def}}{=} \sqrt{\frac{1}{N_t} \sum_{j=1}^{N_t} \left(u_j^{\text{num}}(x^*, y^*, t_j^*) - u_j^{\text{ref}}(x^*, y^*, t_j^*) \right)^2} \quad (24)$$

where N_t is the number of temporal steps and u is the field of interest. Moreover, the uniform norm error ε_{∞} is given by the maximal values of ε_2 :

$$\varepsilon_{\infty} \stackrel{\text{def}}{=} \sup_{x^*, y^* \in [0, 1]} \varepsilon_2(x^*, y^*) \quad (25)$$

Description of the case study

The analytic solution used to the verification is the one presented in [21]. The case study concerns a problem of the Neumann and Dirichlet type. In fact, the left boundary of the body is partially heated through a surface heat flux, while the upper boundary is kept at a constant temperature. All the other surfaces are insulated.

Since the model considers mixed-type boundary conditions, the following set-up is considered in the Spectral-ROM solver. For the insulated boundaries (right and bottom), the Biot coefficients are set to zero $\text{Bi}^B = \text{Bi}^R = 0$. For the top boundary, the Biot coefficient is defined by a large value ($\text{Bi}^T = 10^4$ in our case) with a null ambient field $u_\infty^T = 0$. In this way, the mixed-type conditions from the solver becomes equivalent to a homogeneous Dirichlet) one. Also, the heat flux on the left boundary is applied at $0 \leq y^* \leq 0.5$ and for simulation times $t^* \leq 1$; and the Biot coefficient is set to zero $\text{Bi}^L = 0$.

The temperature is computed as a function of time t^* and space (x^*, y^*) . The geometry of this case study is given in Figure 3. Note that the dimensionless group proposed in this Section is different from the one proposed in [21] for this analytical solution. However, the verification process is not affected since the same dimensionless equations are considered with the same dimensionless parameters for the numerical solution and analytical solution.

Results and discussion

Simulations are performed with $\nu = 1$ and a ratio of $R = 1$ for a time horizon of $\tau^* = 2$, with a time discretization of $\Delta t^* = 1.34 \cdot 10^{-2}$ and spatial discretization parameters for each direction of $\Delta x^* = 10^{-2}$ and $\Delta y^* = 5 \cdot 10^{-3}$. The Spectral-Collocation method is implemented with the same number of modes for both spatial bases, $N = 16$ and $M = 16$, making a total of $N \cdot M = 256$ modes and the final solution is composed for the given spatial grid. In addition, the tolerance of the solver `Matlab™ ode15s` is set to $\text{tol} = 10^{-4}$ which integrates the spectral coefficients in the temporal grid.

This case study allows the heating/cooling process within the material to be analyzed. For this end, Figure 4(a) presents the value of the field u in different locations. The spectral solution seem to be in accordance with the analytical solution at these locations. In addition, Figure 4(b) presents some profiles (also called the fibers of the tensor) of the field u as a function of x^* , at $y^* = 0.4$ and for different instants $t^* = [0.5, 0.8, 1.1]$. In fact, the diffusion process goes from heating to cooling till it reaches the steady state. As observed in the graphics, the

Spectral-Collocation has converged to the analytical solution.

To better evaluate the solutions, the distribution of the error ε_2 among the x^* and y^* axes is presented in Figure 5. The Spectral approach provided a solution with a maximum error of order of $\mathcal{O}(10^{-3})$. For building applications this error is acceptable. Therefore, it can be concluded that the spectral method have converged to the appropriate solution.

Figure 6 presents the temperature as function of x^* and y^* , for a given time instant. Each one of the graphics represents a slice of the discrete tensor solution. It can be observed that the solutions of temperature vary according to both directions x^* and y^* and not only in one direction. If the heat flux were not dependent on the coordinated y^* , the solution would be a false two-dimensional, with variations only in the x^* coordinate.

The main advantage of the Spectral-ROM approach is to reduce the computational resources needed to obtain the solution of the governing equations. The number of degrees of freedom of the Spectral solution is $N \cdot M$, while for a finite-difference methods is $N_x \cdot N_y$. Thus, the degrees of freedom of an Implicit method with central finite-differences discretization would be $2.5 \cdot 10^3$ while for the Spectral collocation is only 81, representing a reduction of 2 orders of magnitude at each time step. Such results imply a reduction of the computational time as presented in Table 2. Even compared to the analytic solution, the computational cost is reduced to 10%. Note that these results have been measured using the `Matlab`TM environment with a computer equipped with Intel i5 CPU (1.6 GHz) and 8 GB of RAM.

Optimal experiment design regarding sensor positioning

The issue is to solve an inverse problem [22, 23] regarding the thermal conductivity λ or its equivalent ν in the dimensionless formulation. To obtain the temperature measurements, a certain number of sensors can be placed in the domain. The issue is to determine the optimal sensor locations. The methodology is described for dimensionless quantities. However, for the sake of clarity, the super script \star is omitted in this Section.

Experiment Design

The total number of sensor locations in the wall is N . The set of all possible labels identifying sensor positions is defined by:

$$J = \{1, \dots, N\} \quad (26)$$

The set of candidate locations is:

$$\Omega_\chi = \{\chi^j\}_{j \in J} \quad (27)$$

where χ^j is a sensor location, so $\chi^j \in [0, l_x] \times [0, l_y]$. The experimental design is illustrated in Figure 7. It consists in positioning n sensors ($n \leq N$) in the wall at the position labels ξ . So, the experimental design is formulated by:

$$\mathcal{D} = \{\xi\}, \quad \xi \subset J \quad (28)$$

where $n = \text{card } \xi$ is the total number of sensors, which is fixed by the user.

Optimal Experiment Design

The optimal experiment design \mathcal{D}° corresponds to the situation where the accuracy of the estimates is maximal. Following the methodology described in [5, 24], the OED is defined by:

$$\mathcal{D}^\circ = \arg \max_{\mathcal{D}} \Phi \quad (29)$$

with Φ being the D-optimum design criterion:

$$\Phi = \log \det \mathbf{M} \quad (30)$$

where \mathbf{M} is the so-called Fisher information matrix. Since there is only one parameter, the matrix has only a single element being:

$$\mathbf{M} = \sum_{j=1}^N w^j \int_0^1 \theta((x, y) = \chi^j, t)^2 dt \quad (31)$$

where $\{w^j\}_{j \in J}$ is the set of binary decision variables (also called design weights) indicating whether or not sensor are placed at the locations labeled by the elements of J :

$$w^j = \begin{cases} 1, & j \in \xi, \\ 0, & j \notin \xi, \end{cases} \quad \forall j \in J \quad (32)$$

Last, the sensitivity coefficients are:

$$\theta = \frac{\partial u}{\partial \nu} \quad (33)$$

which are computed by complex step differentiation. It is important to note that the number of sensors to place n is not a variable of the OED. Indeed, the more sensors are placed the better for the precision. Here, n is fixed (by the experimenter) and only the location of the sensors is investigated. Complementary works investigating the OED for parameter estimation of transfer phenomena in building porous materials can be consulted in [8, 25, 26].

Searching for the OED

The exhaustive search to determine the OED requires to compute the D-optimum criterion for the binomial possibilities $\binom{N}{n}$. This option is too heavy in terms of computational cost for two-dimensional problems. The problem defined by Equation (29) can be seen as an

optimization problem considering the N weighting elements w^j :

$$\mathcal{D} \equiv \{w^j\}_{j \in J} \quad (34)$$

The following constraint must be imposed:

$$\sum_{j=1}^N w^j = n \quad (35)$$

and limiting each design weight to be binary:

$$w^j \in \{0, 1\}, \quad \forall j \in J \quad (36)$$

Such problem can be solved using the genetic algorithm with unknown parameters set as integers. However, these constraints induce an important computational cost as observed in [27] for a one-dimensional problem. Thus, two alternative strategies are investigated to determine the OED.

Strategy 1: optimization of binary design weights using the exchange algorithm

The first strategy consists in solving the problem defined by Equation (29) as an optimization one with binary decision elements. However, an exchange algorithm presented in Table 3 is used [28]. It runs as follows over the iterations k .

Step 1. At $k = 0$, an initial design ξ^0 is selected where $n = \text{card } \xi^0$. For such design, the D-optimum criterion $\Phi(\mathbf{M}(\xi^{(0)}))$ is computed using Equations (30) and (31).

Step 2. The second step consists in exchanging the position labels of the current design with ones that correspond to vacant sites so as to maximally improve the D-optimum criteria. It is performed by determining the labels (i^*, j^*) such that:

$$(i^*, j^*) = \arg \max_{(i,j) \in S^{(k)}} \Delta(i, j) \quad (37)$$

where

$$S^{(k)} = \xi^{(k)} \times (J \setminus \xi^{(k)}) \quad (38)$$

so that $S^{(k)}$ contains all possible exchanges of points, at which a sensor currently resides by points which are currently vacant. The quantity $\Delta(i, j)$ evaluates the relative changes in the D-optimum criterion:

$$\Delta(i, j) = \left(\Phi(\mathbf{M}(\xi_{i \leftrightarrow j})) - \Phi(\mathbf{M}(\xi^{(k)})) \right) \cdot \left(\Phi(\mathbf{M}(\xi^{(k)})) \right)^{-1} \quad (39)$$

where $\xi_{i \leftrightarrow j}$ means the design in which label position i has been replaced by label j .

Step 3. If the relative increase in the D-optimum criterion is lower than a set tolerance

$$\Delta(i^*, j^*) \leq \eta \quad (40)$$

then the algorithm stops since $\xi^{(k)}$ is a locally optimal design. Otherwise, the iterations continues by setting $\xi^{(k+1)} \leftarrow \xi^{(k)}$ and $k \leftarrow k + 1$ and coming back to Step 2.

Strategy 2: optimization via convex relaxation

In the second strategy, the OED is determined using an optimization strategy via convex relaxation. Instead of considering the each design weight as binary, they are relaxed to be any real numbers in the unit interval [29]:

$$w^j \in [0, 1], \quad \forall j \in J \quad (41)$$

As a result, a convenient convex optimization problem is obtained. Then, with determined optimal relaxed weights, the discrete probability distribution of each position sensor can be

assessed by:

$$\mathcal{P}^j = w^j \cdot \left(\sum_{j=1}^N w^j \right)^{-1} \quad (42)$$

Such problem is solved using the interior point algorithm in the `Matlab`TM environment.

Case study

The problem involves heat transfer through the façade of a building located in the urban area of Paris, where the studied building faces another one. The front building induces a time varying shadow on the studied building. The heat flux in the façade varies vertically according with the position of the sun the wind velocity justifying the two dimensional simulation. Details of the case study are given in [30].

Description of the case study

The geometry of this case study is given in Figure 7. The case study considers a south-oriented façade of a building located in Paris, France. The wall is composed of a concrete layer, whose material properties are given by the following values: $\lambda = 1.4 \text{ W} \cdot \text{m}^{-1} \cdot \text{K}^{-1}$ for the thermal conductivity, $\rho = 2 \cdot 10^3 \text{ kg} \cdot \text{m}^{-3}$ for the density, and, $c_p = 10^3 \text{ J} \cdot \text{kg}^{-1} \cdot \text{K}^{-1}$ for the specific heat capacity. The height and width of the wall are $l_y = 3 \text{ m}$ and $l_x = 30 \text{ cm}$. The façade is located in an urban area so it is facing other buildings. The latter is located at a distance of 5 m and has a height of 3 m , which induces a shadow on the studied façade. The height of the shadow varies according to time. As a consequence, the outside incident radiation flux q_∞ , varies according to height and time. The radiate absorption coefficient is set as $\alpha = 0.6$. The outside surface heat transfer coefficient h^L depends on height position y and time varying climate wind velocity. The surface heat transfer coefficient increases according to the height.

The outside temperature is also given by weather data file and illustrated in Figure 8(a). The inside temperature is controlled and set to 20°C. The inside surface transfer coefficient is set as constant to $h^R = 10 \text{ W} \cdot \text{m}^{-2} \cdot \text{K}^{-1}$. The top and bottom boundaries of the façade are set as adiabatic ($h^T = h^B = 0$). Indeed, the investigations focus on the influence of the space and time variations of outside boundary conditions on the thermal efficiency of the façade. The simulation is performed for January, with a time horizon of $\tau = 31$ days . During this period, the influence of the urban scene is more noticeable. Figure 8(b) shows the variation of the sunlit height for each days of the month. The shadow covers all the façade during the night ($h = 3 \text{ m}$). At midday the height is around 1.5 m and 1 m at the beginning and the end of the month, respectively. This variation of the sunlit height induces spatial variation of the incident flux as presented in Figure 8(c). At the top of the façade, the magnitude of the flux is higher. Last, the surface transfer coefficient also varies according to space and time as shown in Figure 8(d).

For the experimental design, a total of $N = 2086$ candidate sensor positions are possible in the whole façade. This value is obtained by constraining a minimum gap of 2 cm between two neighboring sensors and avoiding sensors at the interfaces with inside/outside air. So, given the height and wide to the façade, it corresponds to 14 possible locations along x axis and to 149 possible locations along y axis. The strategy via convex relaxation is employed to determine the OED. Tolerances of optimization solvers are set to 10^{-8} .

Results and discussion

Simulations are performed for $\nu = 2.8 \cdot 10^{-2}$ and $R = 10^{-2}$, for a time horizon of $\tau^* = 744$, with a spatial discretization parameters for each direction of $\Delta x^* = 10^{-2}$ and $\Delta y^* = 2 \cdot 10^{-3}$. The Spectral-Collocation method is implemented with the same number of modes for both spatial bases, $N = 11$ and $M = 11$, making a total of $N \cdot M = 121$ modes and the final solution is composed for the given spatial grid. In addition, the tolerance of the solver `ode15s` is set to $\text{tol} = 10^{-4}$ which integrates the spectral coefficients in the temporal grid. The time

discretization is $\Delta t^* = 1 \cdot 10^{-1}$ for projecting the solution. The reference values for the dimensionless quantities are $T_{\text{ref}} = 293.15 \text{ K}$, $\Delta T_{\text{ref}} = 50 \text{ K}$ and $t_{\text{ref}} = 3600 \text{ s}$.

First, the number of sensor to place is set to $n = 5$. Results of the OED are given in Table 4 for both strategies. The optimal location on x axis is the same for all sensors ($x = 0.10 \text{ m}$). On the y axis, the sensors should be placed in the same region around 2.52 m . Both strategies give the exact same results. The convex strategy enables to assess complementary information which is the probability of sensor placement as shown in Figure 9(a). The probability is very sharp in the region around 2.52 m . Figure 10 presents the variation of the probability with the number of sensor n . The probability remains very sharp in the region $x = 0.1\text{m}$ and 2.52 m . The optimal location does not change much according to the number of sensors.

This area corresponds to the top of the façade, where the incident radiation flux has a higher magnitude. The sensitivity coefficients have a higher magnitude as presented in Figure 11. Those results are due to the influence of the two-dimensional modeling of the façade boundary conditions. Figure 12(a) presents the evolution of the temperature for two different locations, at ($x = 0.1 \text{ m}$, $y = 2.5 \text{ m}$) and at ($x = 0.28 \text{ m}$, $y = 0.24 \text{ m}$). The influence of the sun is remarked during midday with the high peaks differences. In addition, Figure 12(b) presents the slice of the solution for January 15, at 12:00. As a consequence of the shadow, the bottom of the façade receives less flux, which makes temperatures lower in this part. The optimal sensors locations are indicated by the dots.

Figure 9(b) shows the experimental design determined using the first strategy with the exchange algorithm according to the iteration number (with $n = 5$ sensors to place). Since the algorithm may found a local optimal solution, several tests have been performed for different set of initial guess. For all the tests, the strategy converges to the same OED. At each iteration, only one sensor position is changed as set in the algorithm. Very few iterations are required for the algorithm to determine a local optimal solution.

Figure 13 presents the variation of the design criterion according to the number of sensors. As expected from the theoretical results, it increases monotonously with n . Thus, the more

sensors are placed, the better for the precision. The number of sensors can be chosen using such figure by analyzing the compromise between the precision of estimation and the experimental constraints such as cost, design difficulties, etc. Regarding the accuracy, the domain $n \in [5, 10]$ seems relevant since the slope of the curve starts to decrease. Note that in the hypothetical situation where $n \rightarrow N$, necessarily some sensors will be placed in some regions of low sensitivity. It is due to the constrain in the experimental design that two sensors cannot be placed in the same locations (no overlapping).

The exhaustive search for $n = 5$ scales with more than $300 \cdot 10^{12}$ possibilities (binomial coefficient $\binom{2086}{5}$ exactly) which is unreliable in terms of computation cost. A comparison of the cost function evaluation among the strategies is reported in Table 5. The exchange algorithm strategy is the one with the smallest cost function evaluations. The latter is computed as follows. At each iteration, the algorithm requires to evaluate the D-optimum criteria (30) for the designs ξ^k and $\xi_{i \leftrightarrow j}$. The total cost function evaluation is at each iteration:

$$1 + n \cdot \binom{N-n}{1} \quad (43)$$

which gives for $n = 5$, 10 406 evaluations of the criterion. At each iteration, the algorithm computes the D-optimum criterion for the design ξ^k (1 evaluation) and the designs $\xi_{i \leftrightarrow j}$. For the latter, the possibilities are changing one sensor location among the $N - n$ remaining positions. So $\binom{N-n}{1}$ evaluations of the criterion. Since each of the n sensors can move, it leads to $n \cdot \binom{N-n}{1}$ evaluations for the designs $\xi_{i \leftrightarrow j}$. In the end, the ratio compared to the exhaustive search scales with $\mathcal{O}(10^{-8})$. The optimization strategy with integer decision elements enables to retrieve the OED with ten times more cost function evaluations. It corresponds to a ratio of $1.6 \cdot 10^{-7}$ with the exhaustive approach. It shows a satisfying efficiency of the approach noting that an optimal relaxed weight is obtained.

Conclusions

This article proposes the search for the OED in terms of sensor positioning in a wall façade for a thermal conductivity inverse two-dimensional heat transfer problem. The direct problem is solved using a reduced spectral method. It is verified using an analytical solution, highlighting a satisfactory accuracy and computational cost. Then, the OED is investigated by solving an optimization problem of the D-optimum criterion considering two strategies. The first one is based on an exchange algorithm. For the second strategy, a convex relaxation approach is adopted. The decision elements to place the sensors are considered as real number in the unit interval. A (discrete) probability distribution of the sensor position is obtained. The first strategy is the most efficient from a computational point of view. In a few iterations, an local optimal solution is retrieved. The convex relaxation has a higher computational cost but still very low compared to the exhaustive search. Furthermore, it provides complementary probabilistic information for the experimenter. Future works should focus on multi-layer configurations with the thermal conductivity of each layer to retrieve.

Acknowledgments

The authors acknowledge the DSG 2021 project TOPS for the financial support.

Conflict of interests

The authors declare that they have no known competing financial interests or personal relationships that could have appeared to influence the work reported in this paper.

Nomenclature

a, b	spectral coefficient
A, C, D, \mathcal{M}	spectral matrices
Bi	Biot number
c	constant
c_p	specific heat, $\text{J} \cdot \text{kg}^{-1} \cdot \text{K}^{-1}$
CPU	Central Processing Unit
\mathcal{D}	experimental design
DOF	Degree of freedom
f	generic function
GB	GigaByte
h	heat transfer coefficient, $\text{W} \cdot \text{m}^{-2} \cdot \text{K}^{-1}$
h	shadow height, m
Id	identity matrix
i, j	label position
J	set of label position
k	iterations
l_x, l_y	length of facade, m
M	Fisher information matrix
N	number of sensor position
N, M	order of the Spectral decomposition
n	number of sensors

OED	Optimal Experiment Design
\mathcal{O}	order of a scalar quantity
\mathcal{P}	discrete probability distribution of position sensor
q	solar radiation flux, $\text{W} \cdot \text{m}^{-2}$
R	ratio
\mathcal{R}	residual
RAM	Random Access Memory
ROM	Reduced Order Model
S	Set of all possible exchanges of points
t	time, s
tol	Tolerance
$T, \Delta T$	temperature, K
T	Chebyshev polynomials
u	dimensionless temperature
w	binary decision variables for sensor position
x, y	coordinates

Greek symbols

α	solar absorptivity
Δ	improvement in the D–optimum criteria
$\Delta x, \Delta y, \Delta t$	discretisation parameters
ε	error
η	tolerance parameter
θ	dimensionless sensitivity coefficient
λ	thermal conductivity, $\text{W} \cdot \text{m}^{-1} \cdot \text{K}^{-1}$
τ	horizon of simulation, s
ν	dimensionless diffusivity
ξ	set of label position
ρ	density, $\text{kg} \cdot \text{m}^{-3}$
Φ	D–optimum design criterion
χ	sensor location, m
Ω	set of candidate locations for sensor position

Subscripts

cpu	Central Processing Unit
ref	reference condition
x	according to x coordinate
y	according to y coordinate
0	initial condition
2	Euclidean norm
∞	ambient air condition
\boxtimes	uniform norm
χ	sensor position

Superscripts

B	bottom boundary
$i \leftrightarrow j$	exchange of label i by label j
L	left boundary
R	right boundary
T	top boundary
x	according to x coordinate
y	according to y coordinate
0	first iteration
\circ	optimal
\star	dimensionless quantity
$*$	labels that improved the design
\sim	first order derivative
\approx	second order derivative
$-$	canonical interval

References

- [1] L. Laurenti, F. Marcotullio, and F. de Monte. Determination of the thermal resistance of walls through a dynamic analysis of in-situ data. *International Journal of Thermal Sciences*, vol. 43, no. 3, pp. 297–306, 2004. [doi:10.1016/j.ijthermalsci.2003.08.007](https://doi.org/10.1016/j.ijthermalsci.2003.08.007).
- [2] J.V. Beck and K.J. Arnold. *Parameter Estimation in Engineering and Science*. James Beck, New York, NY, John Wiley and Sons edition, 1977.
- [3] L. Pronzato and A. Pázman. *Design of Experiments in Nonlinear Models*. Number 0930-

- 0325 in Lecture Notes in Statistics. New York, NY, Springer edition, 2019. URL: <https://link.springer.com/book/10.1007/978-1-4614-6363-4>.
- [4] A. Nenarokomov and D.V. Titov. Optimal experiment design to estimate the radiative properties of materials. *J. of Quant. Spectroscopy and Rad. Transfer*, vol. 93, no. 1, pp. 313–323, 2005. doi:10.1016/j.jqsrt.2004.07.036.
- [5] G. D’Alessandro and F. de Monte. On the Optimum Experiment and Heating Times when Estimating Thermal Properties through the Plane Source Method. *Heat Transf. Engineering*, vol. 43, no. 3-5, pp. 257–269, 2022. doi:10.1080/01457632.2021.1874655.
- [6] G. D’Alessandro and F. de Monte. Optimal experiment design for thermal property estimation using a boundary condition of the fourth kind with a time-limited heating period. *Int. J. Heat Mass Transf.*, vol. 134, pp. 1268–1282, 2019. doi:10.1016/j.ijheatmasstransfer.2019.02.035.
- [7] E. A. Artyukhin and S. A. Budnik. Optimal planning of measurements in numerical experiment determination of the characteristics of a heat flux. *Journal Eng. Physics*, vol. 49, no. 6, pp. 1453–1458, 1985. doi:10.1007/BF00871299.
- [8] A. Jumabekova, J. Berger, A. Fouquier, and G.S. Dulikravich. Searching an optimal experiment observation sequence to estimate the thermal properties of a multilayer wall under real climate conditions. *Int. J. Heat Mass Transf.*, vol. 155, page 119810, 2020. doi:10.1016/j.ijheatmasstransfer.2020.119810.
- [9] M. Bazargani and F. Kowsary. Methodology for estimation of local convective heat transfer coefficient for vapor condensation. *Heat Transf. Eng.*, vol. 36, no. 9, pp. 820–828, 2015. doi:10.1080/01457632.2015.963420.
- [10] J.R. Howell, M.P. Menguc, and R. Siegel. *Thermal Radiation Heat Transfer, 5th Edition*. Boca Raton, FL: CRC Press, 2010. URL: <https://books.google.fr/books?id=FBjSBQAAQBAJ>.

- [11] C. Canuto, M. Y. Hussaini, A. Quarteroni, and T. A. Zang. *Spectral Methods in Fluid Dynamics*. Springer series in computational physics. Springer-Verlag, 1988. URL: <https://link.springer.com/book/10.1007%2F978-3-642-84108-8#about>, doi:10.1007/978-3-642-84108-8.
- [12] S. Gasparin, D. Dutykh, and Nathan Mendes. A spectral method for solving heat and moisture transfer through consolidated porous media. *International J. Num. Methods in Eng.*, vol. 117, no. 11, pp. 1143–1170, 2019. doi:10.1002/nme.5994.
- [13] R. Peyret. *Spectral methods for incompressible viscous flow*. Springer, New York, 2002.
- [14] B. Fornberg. *A practical guide to pseudospectral methods*. Cambridge University Press, New York, USA, 1996.
- [15] F. Liu, X. Ye, and X. Wang. Efficient Chebyshev spectral method for solving linear elliptic PDEs using quasi-inverse technique. *Num. Math.: Theory, Meth. and Applications*, vol. 4, no. 2, pp. 197–215, 2011. doi:10.1017/S100489790000060X.
- [16] T. Kolda and B. Bader. Tensor decompositions and applications. *SIAM Review*, vol. 51, no. 3, pp. 455–500, 2009. arXiv:<https://doi.org/10.1137/07070111X>, doi:10.1137/07070111X.
- [17] R. Peyret. *Spectral methods for incompressible viscous flow*. Springer, New York, 2002.
- [18] J. P. Boyd. *Chebyshev and Fourier Spectral Methods*. Dover Publications, New York, second edition edition, 2000.
- [19] ASME V&V and Committee Members. *ASME V&V 20-2009 Standard for Verification and Validation in Computational Fluid Dynamics and Heat Transfer (V&V20 Committee Chair and principal author)*, volume 20. New York, american society of mechanical engineering edition, 2009.

- [20] P. J. Roache. Code Verification by the Method of Manufactured Solutions . *Journal of Fluids Engineering*, vol.124, no 1. pp 4–10, 2001. doi:[10.1115/1.1436090](https://doi.org/10.1115/1.1436090).
- [21] R. L. McMasters, F. de Monte, G. D’Alessandro, and J. V. Beck. Verification of ansys and matlab Heat Conduction Results Using an “Intrinsically” Verified Exact Analytical Solution. *J. Verification, Validation and Uncertain. Quant.*, vol. 6, no. 2, pages 21005, 2021. doi:[10.1115/1.4050610](https://doi.org/10.1115/1.4050610).
- [22] C. A. A. Mota, H. R. B. Orlande, M.O. M. De Carvalho, V. Kolehmainen, and J. P. Kaipio. Bayesian Estimation of Temperature-Dependent Thermophysical Properties and Transient Boundary Heat Flux. *Heat Transfer Eng.*, vol. 31, no. 7, pp. 570–580, Jul. 2010. doi:[10.1080/01457630903425635](https://doi.org/10.1080/01457630903425635).
- [23] V. Tahmasbi and S. Noori. Application of Levenberg–Marquardt Method for Estimation of the Thermophysical Properties and Thermal Boundary Conditions of Decomposing Materials. *Heat Transf. Eng.*, vol. 41, no. 5, pp. 449–475, 2020. doi:[10.1080/01457632.2018.1558010](https://doi.org/10.1080/01457632.2018.1558010).
- [24] D. Ucinski. *Optimal Measurement Methods for Distributed Parameter System Identification*. Boca Raton, FL: CRC Press, 2004.
- [25] J. Berger and B. Kadoch. Estimation of the thermal properties of an historic building wall by combining modal identification method and optimal experiment design. *Build. and Environ.*, vol. 185, page 107065, 2020. doi:[10.1016/j.buildenv.2020.107065](https://doi.org/10.1016/j.buildenv.2020.107065).
- [26] J. Berger, T. Busser, D. Dutykh, and N. Mendes. An efficient method to estimate sorption isotherm curve coefficients. *Inverse Probl. in Sc. and Eng.*, vol. 27, no. 6, pp. 735–772, 2019. doi:[10.1080/17415977.2018.1495720](https://doi.org/10.1080/17415977.2018.1495720).
- [27] J. Berger, S. Gapasrin, and D. Uciński. Optimal sensor location ofr inverse heat conduction problem in multilayered building walls. In *2022 Société Française de Thermique (SFT) conference*, pages 1–8, 2022.

- [28] A. Atkinson, A. Donev, and R. Tobias. *Optimum Experimental Designs, with SAS*. Oxford Statistical Science Series. Oxford University Press, Oxford, New York, 2007.
- [29] D. Ucinski. E-optimum sensor selection for estimation of subsets of parameters. *Measurement*, 187:110286, 2022. [doi:10.1016/j.measurement.2021.110286](https://doi.org/10.1016/j.measurement.2021.110286).
- [30] J. Berger, S. Gasparin, W. Mazuroski, and N. Mendes. An efficient two-dimensional heat transfer model for building envelopes. *Num. Heat Transf., Part A: Applications*, vol. 79, no. 3, pp. 163–194, Nov. 2020. [doi:10.1080/10407782.2020.1836936](https://doi.org/10.1080/10407782.2020.1836936).

Appendix

Comparison test of the Spectral-ROM

The case considers adiabatic top and bottom boundaries (so $\text{Bi}^T = \text{Bi}^B = 0$). For the right boundary condition, the ambient field varies according to time and space:

$$u_{\infty}^R(y^*, t^*) = 1.3 \sin\left(\frac{\pi}{24} t^*\right) - 1.8(y^* - 1)y^*,$$

The Biot coefficient is set to $\text{Bi}^R = 1$. For the left boundary, an incident radiation flux is imposed varying also with time and space, as for real configurations:

$$q_{\infty}^*(y^*, t^*) = 1.3 y^* \sin\left(\frac{\pi}{12} t^*\right)^2.$$

The Biot coefficient is set to $\text{Bi}^L = 0$.

Simulations are performed with $\nu = 10^{-4}$ and a ratio of $R = 1$ for a time horizon of $\tau^* = 12$, with a time discretization of $\Delta t^* = 10^{-1}$ and spatial discretization parameters for each direction of $\Delta x^* = 10^{-2}$ and $\Delta y^* = 5 \cdot 10^{-3}$. The Spectral-Collocation method is implemented with the same number of modes for both spatial bases, $N = 9$ and $M = 9$, making a total of $N \cdot M = 81$ modes and the final solution is composed for the given spatial grid. In addition, the tolerance of the solver `Matlab™ ode15s` is set to $\text{tol} = 10^{-4}$ which integrates the spectral coefficients in the temporal grid. The comparison is carried out with the alternating-direction implicit method [30] for the same discretization parameters. Figures 14(a), 14(b) and 15 shows a very good agreement among the solutions. The error scales with $\mathcal{O}(10^{-3})$ as presented in Figure 16. This additional comparison leads to a complementary verification of the accuracy of the Spectral-ROM solver.

Table 1. *Spectral-Collocation's algorithm for composing $f(t, a_{ij})$ and \mathcal{M} .*

```

1 :  $f := \text{zeros}(N \cdot M, 1)$ 
2 :  $\mathcal{M} := \text{zeros}(N \cdot M, N \cdot M)$ 
3 : for  $k = 0$        $\triangleright$  Collocation point  $\bar{x}_0 = -1$ 
4 :     for  $l = 0 : M - 1$ 
5 :          $f[l] := [C(-1) \otimes C(\bar{y}_l)] \cdot A_{ij} - u_\infty^L(t)$        $\triangleright$  Equation (21a)
6 :     end
7 : end
8 : for  $k = 1, 2, \dots, N - 2$        $\triangleright$  Internal  $\bar{x}_k$  collocation points
9 :     for  $l = 0$ 
10 :         $f[(M - 1)k + 1] := [C(\bar{x}_k) \otimes C(-1)] \cdot [(\mathbf{Id}_x \otimes \tilde{D}_y) \cdot A_{ij}]$        $\triangleright$  Equation (21c)
11 :    end
12 :    for  $l = 1, 2, \dots, M - 2$ 
13 :         $f[(M - 1)k + l] := [C(\bar{x}_k) \otimes C(\bar{y}_l)] \cdot [(\alpha_y \cdot \mathbf{Id}_x \otimes \tilde{D}_y + \alpha_x \cdot \tilde{D}_x \otimes \mathbf{Id}_y) \cdot A_{ij}]$ 
14 :             $\triangleright$  Right side of Equation (18)
15 :    end
16 :    for  $l = M - 1$ 
17 :         $f[(M - 1)k + (M - 1)] := [C(\bar{x}_k) \otimes C(+1)] \cdot [(\mathbf{Id}_x \otimes \tilde{D}_y) \cdot A_{ij}]$ 
18 :             $\triangleright$  Equation (21d)
19 :    end
20 : end
21 : for  $k = N - 1$        $\triangleright$  Collocation point  $\bar{x}_{M-1} = 1$ 
22 :     for  $l = 0 : M - 1$ 
23 :          $f[l + (M - 1) \cdot (N - 2)] := [C(+1) \otimes C(\bar{y}_l)] \cdot A_{ij} - u_\infty^R(t)$        $\triangleright$  Equation (21b)
24 :     end
25 : end
26 : return  $f(t, a_{ij})$  and  $\mathcal{M}$ .

```

Table 2. *Features of the Analytic and Spectral solution for the verification case.*

<i>Method</i>	Δt^*	Δx^*	Δy^*	tol	ε_{\boxtimes}	DOF	t_{cpu}	R_{cpu}
<i>Analytic</i>	$1.3 \cdot 10^{-2}$	10^{-2}	$5 \cdot 10^{-3}$	—	—	10^4	117 s	100 %
<i>Spectral</i>	$1.3 \cdot 10^{-2}$	10^{-2}	$5 \cdot 10^{-3}$	10^{-4}	$\cdot 10^{-3}$	10^2	12 s	10 %

Table 3. *Exchange algorithm to determine the OED using Strategy 1.*

1 :	Sample candidate design ξ^0	\triangleright <i>Step 1</i>
2 :	Compute D-optimum criteria $\Phi(\mathbf{M}(\xi^{(0)}))$	
3 :	$k = 0$	
4 :	While $\Delta(i^*, j^*) \geq \eta$	
5 :	State S^k	\triangleright <i>Step 2</i>
6 :	Determine labels (i^*, j^*) according to Equation (37)	
7 :	Compute $\Delta(i^*, j^*)$ with Equation (39)	
8 :	$k = k + 1$	
9 :	End	
10 :	return OED $\mathcal{D}^\circ = \{\xi^{k-1}, n\}$	

Table 4. *Optimal Experiment design for $n = 5$ sensor positions (given in m).*

	χ^1		χ^2		χ^3		χ^4		χ^5	
<i>Strategy</i>	<i>x</i>	<i>y</i>	<i>x</i>	<i>y</i>	<i>x</i>	<i>y</i>	<i>x</i>	<i>y</i>	<i>x</i>	<i>y</i>
Exchange algorithm	0.10	2.5	0.10	2.52	0.10	2.54	0.10	2.56	0.10	2.58
Convex strategy	0.10	2.5	0.10	2.52	0.10	2.54	0.10	2.56	0.10	2.58

Table 5. *Function count to determine the Optimal Experiment design according to the different strategies.*

<i>Strategy</i>	<i>Number</i>	<i>Ratio %</i>
Exhaustive search	$\binom{2086}{5}$	1
Exchange algorithm	52 030	$\mathcal{O}(10^{-8})$
Convex strategy	477 939	$\mathcal{O}(10^{-7})$

List of Figures

- 1 Illustration of the problem under investigation.
- 2 Representation of the two-dimensional collocation points.
- 3 Geometry of test body [21].
- 4 Evolution of the dimensionless temperature field u (a) and some profiles at different time instants (b).
- 5 Error ε_2 as function of x^* and y^* axes.
- 6 Slices of the solution for the time instant $t = 0.5$ h.
- 7 Configuration of the case study for Paris weather.
- 8 Time evolution of the outside/inside temperature (a) of the sunlit height on the façade (b) of the incident radiation flux (c) and of the outside surface heat transfer coefficient (d).
- 9 Probability of the sensor placement considering real decision elements along the y axis ($x = 0.10$ m) obtained with (Strategy 2) (a). Variation of the selected design of the exchange algorithm (Strategy 1) according to the iterations (b).
- 10 Variation of the probability of the sensor placement according to the number of sensors
- 11 Time evolution of the sensitivity coefficients at an optimal and non-optimal sensor location.
- 12 Evolution of the dimensionless temperature field (a) and slice of the solution for January 15 at 12:00, with the sensors locations indicated in red dots (b).
- 13 Variation of the D-optimum design criterion with the number of sensors n .
- 14 Evolution of the dimensionless temperature field u (a) and some profiles at different time instants for $y^* = 0.9$ (b).
- 15 Slices of the solution for the time instant $t^* = 6$.
- 16 Error ε_2 as function of x^* and y^* axes.

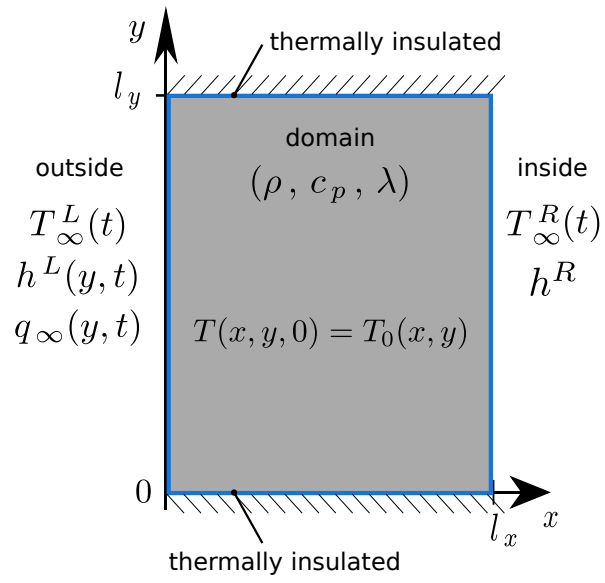


Figure 1. *Illustration of the problem under investigation.*

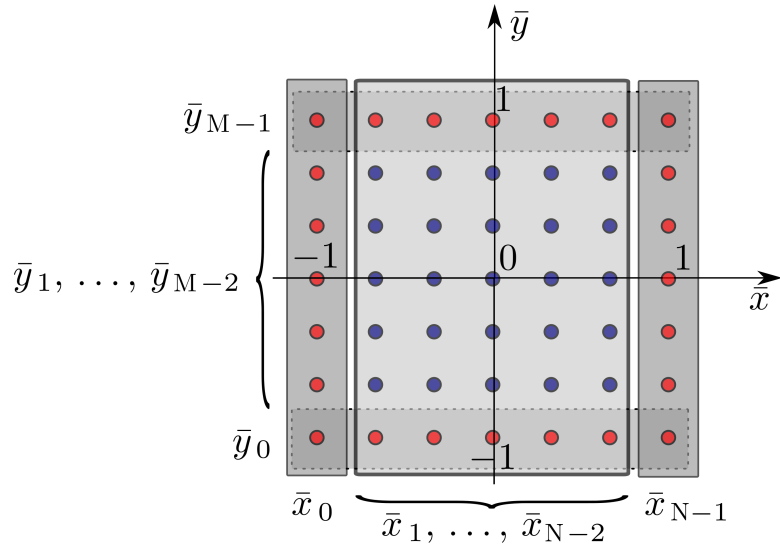


Figure 2. *Representation of the two-dimensional collocation points.*

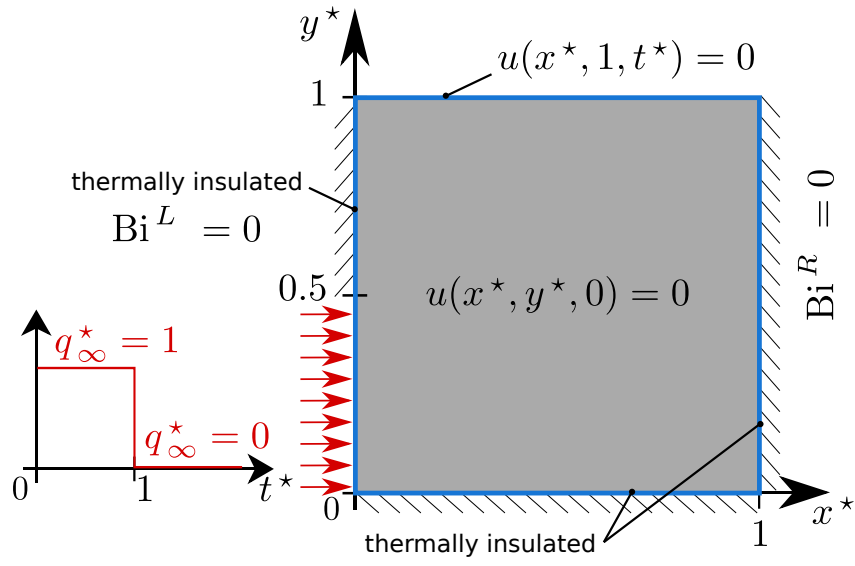


Figure 3. *Geometry of test body [21].*

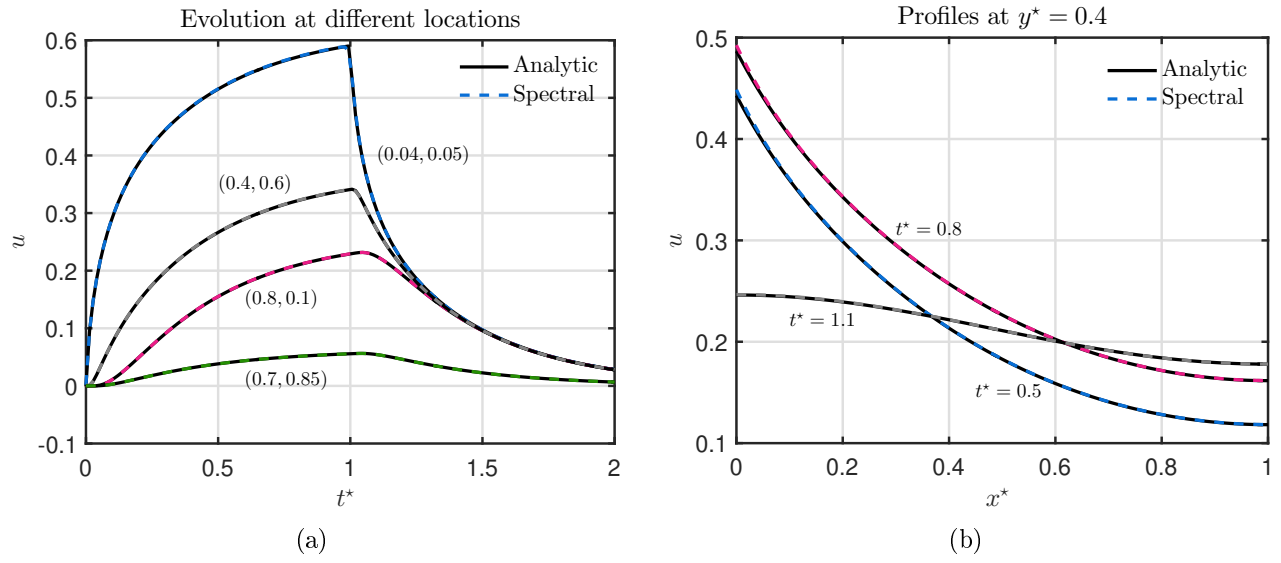


Figure 4. Evolution of the dimensionless temperature field u (a) and some profiles at different time instants (b).

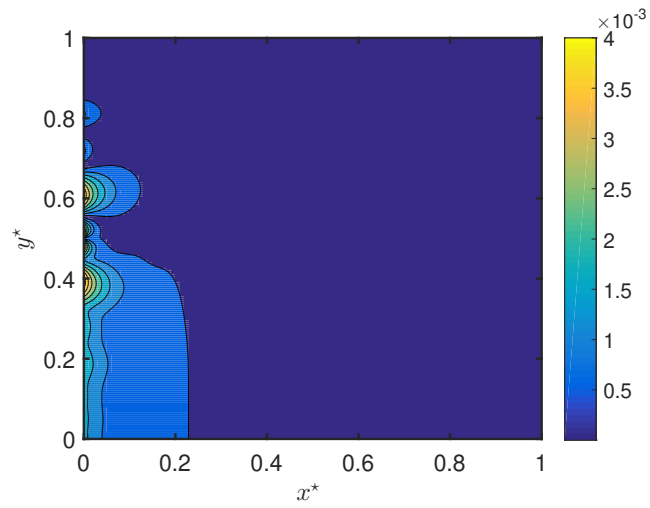


Figure 5. *Error ε_2 as function of x^* and y^* axes.*

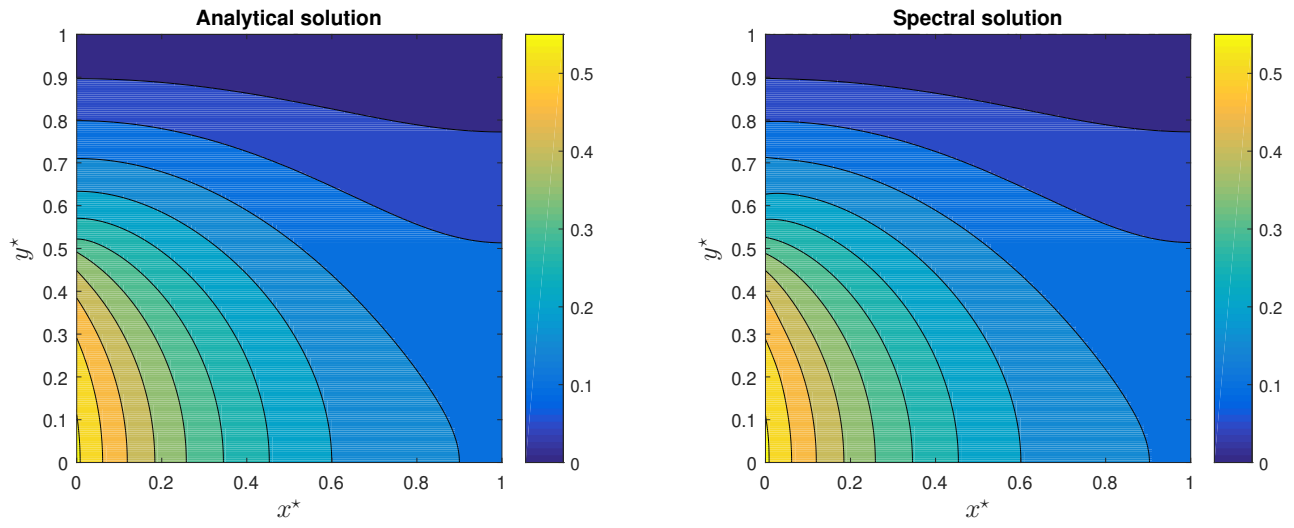


Figure 6. *Slices of the solution for the time instant $t = 0.5$ h.*

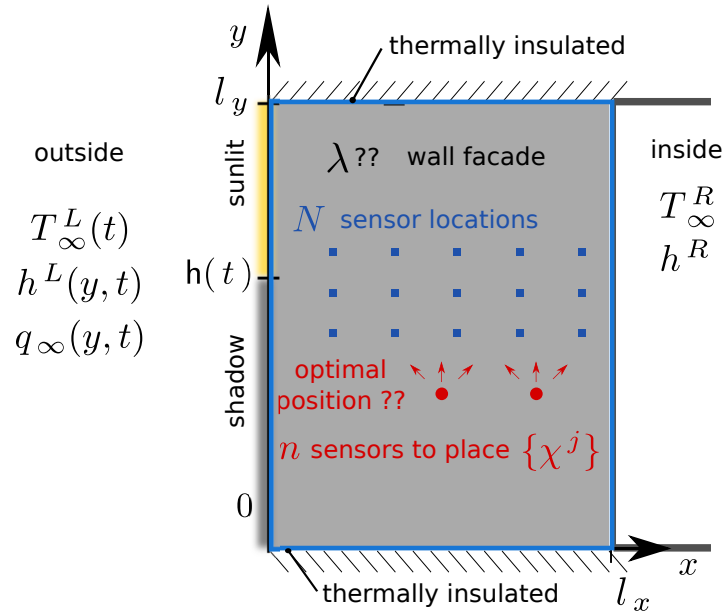


Figure 7. Configuration of the case study for Paris weather.

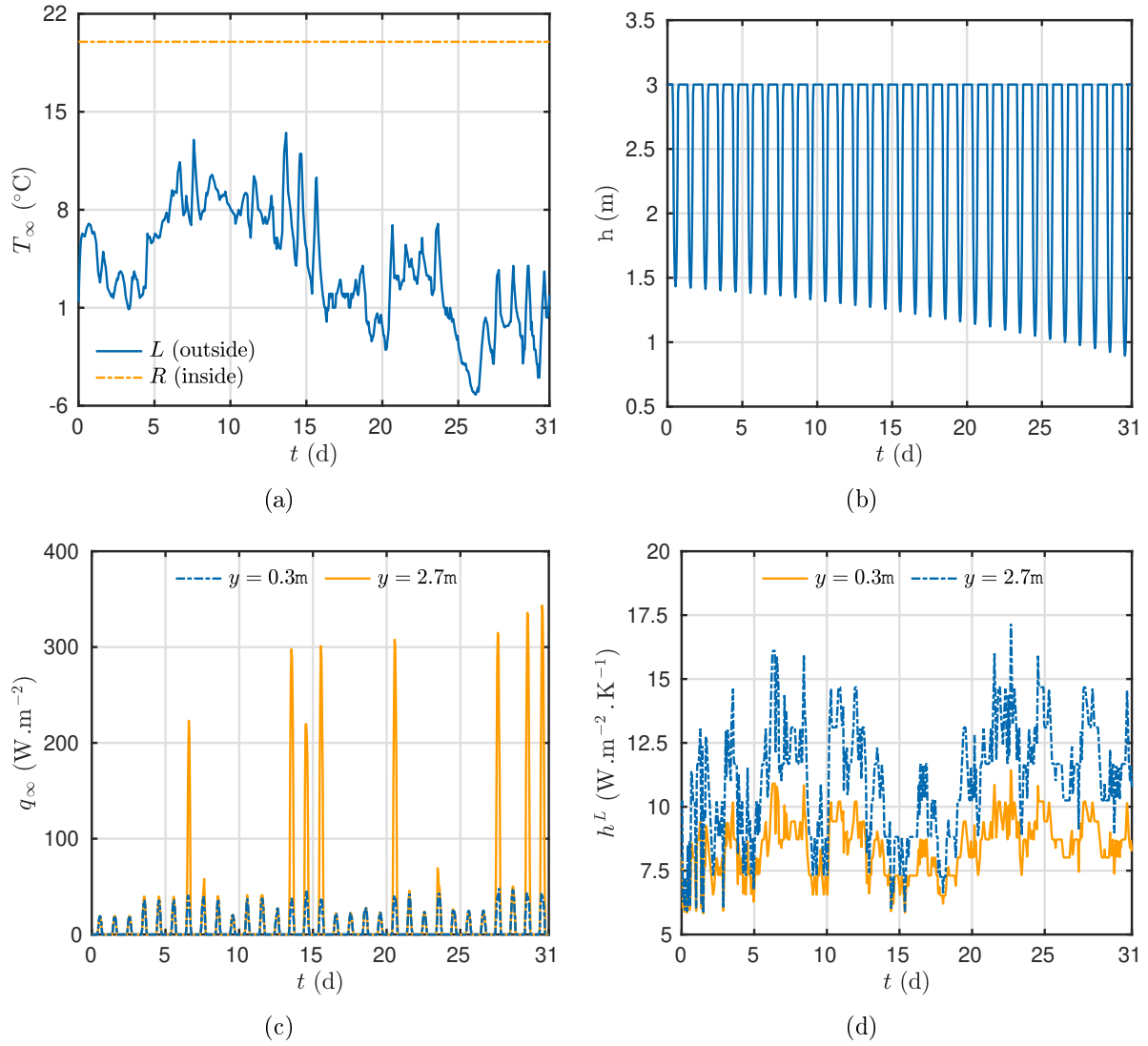


Figure 8. Time evolution of the outside/inside temperature (a) of the sunlit height on the façade (b) of the incident radiation flux (c) and of the outside surface heat transfer coefficient (d).

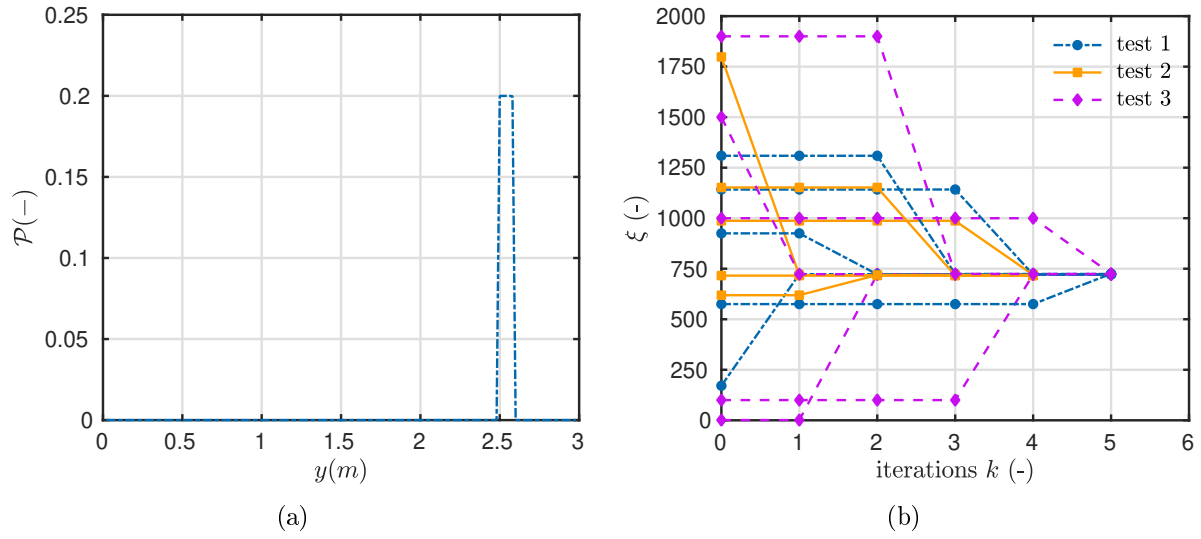


Figure 9. Probability of the sensor placement considering real decision elements along the y axis ($x = 0.10$ m) obtained with (Strategy 2) (a). Variation of the selected design of the exchange algorithm (Strategy 1) according to the iterations (b).

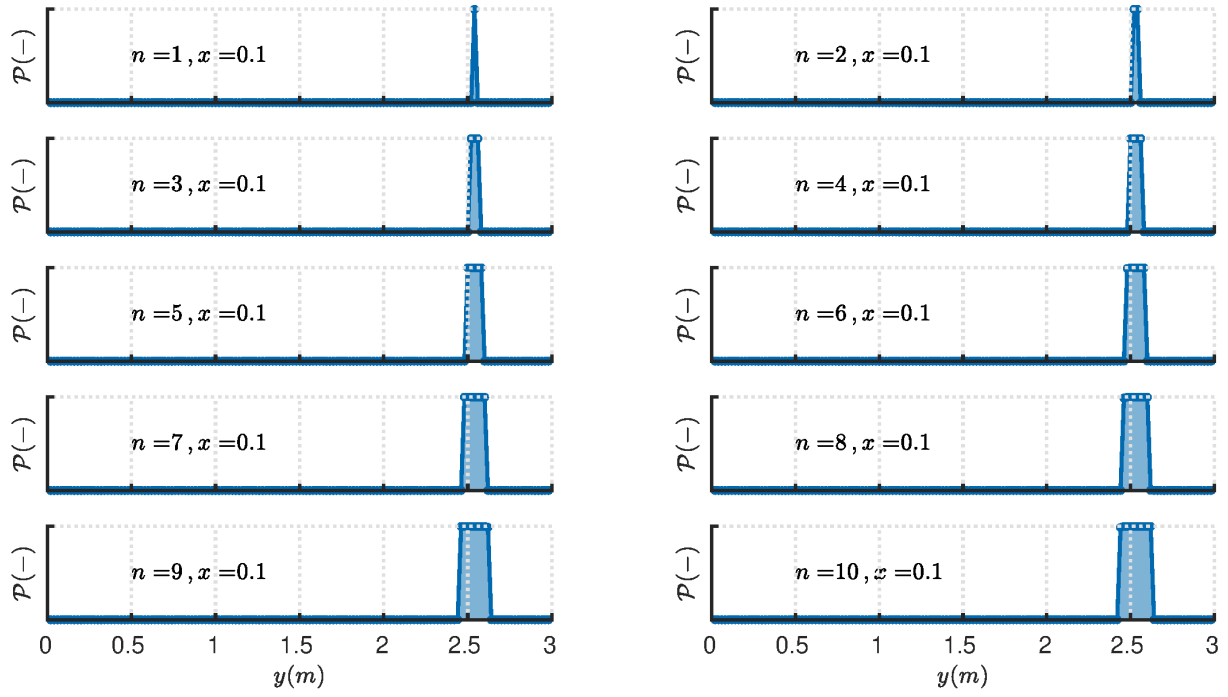


Figure 10. *Variation of the probability of the sensor placement according to the number of sensors*

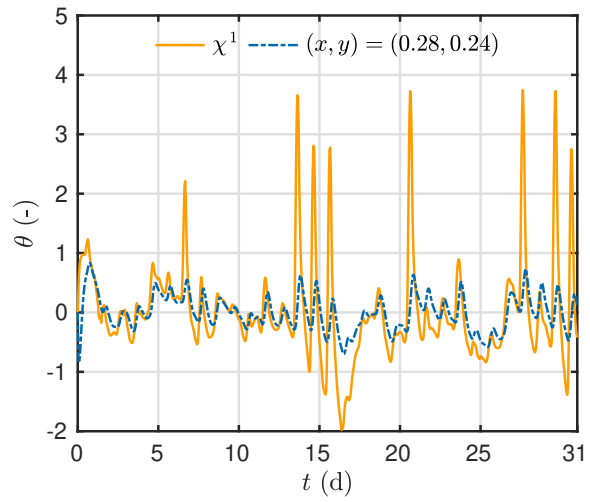


Figure 11. *Time evolution of the sensitivity coefficients at an optimal and non-optimal sensor location.*

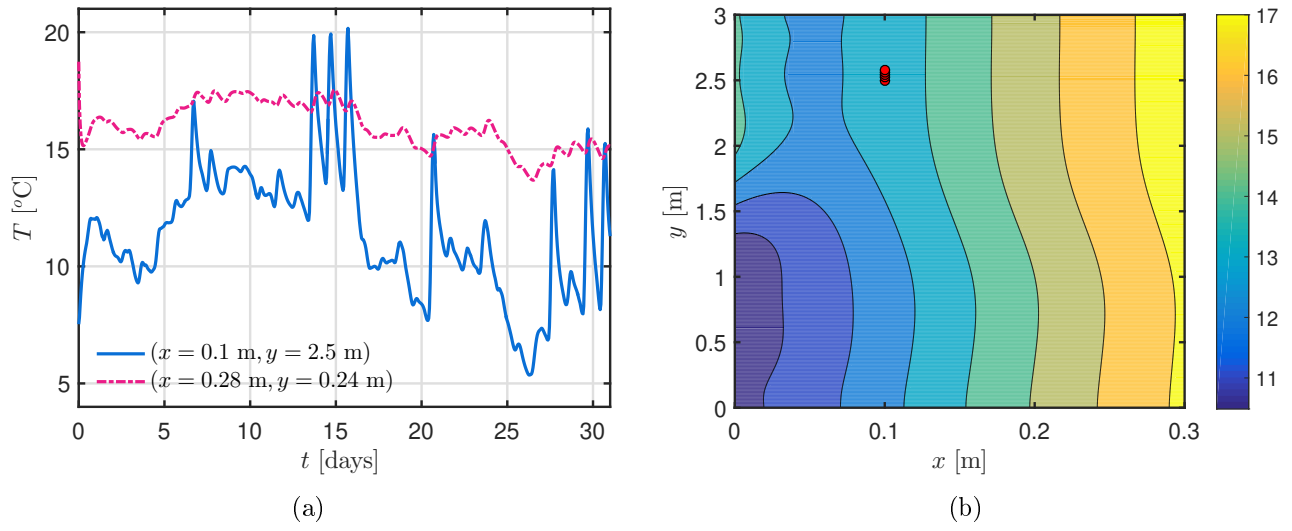


Figure 12. *Evolution of the dimensionless temperature field (a) and slice of the solution for January 15 at 12:00, with the sensors locations indicated in red dots (b).*

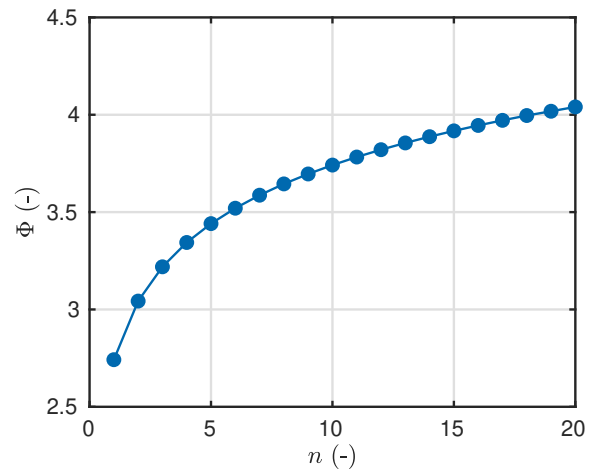


Figure 13. *Variation of the D-optimum design criterion with the number of sensors n .*

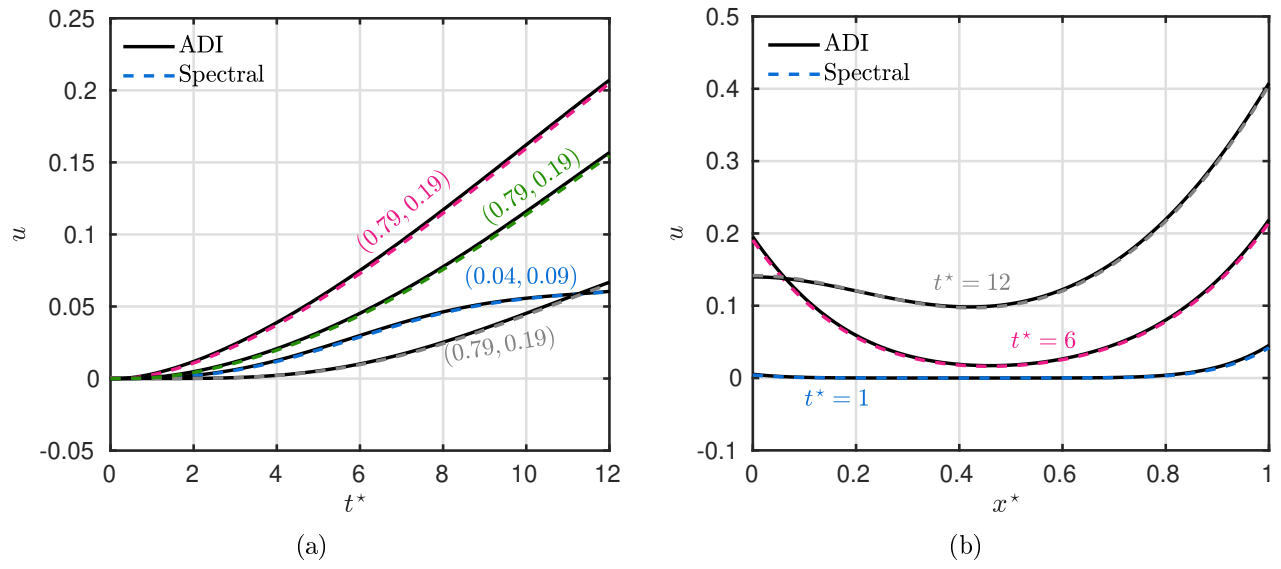


Figure 14. Evolution of the dimensionless temperature field u (a) and some profiles at different time instants for $y^* = 0.9$ (b).

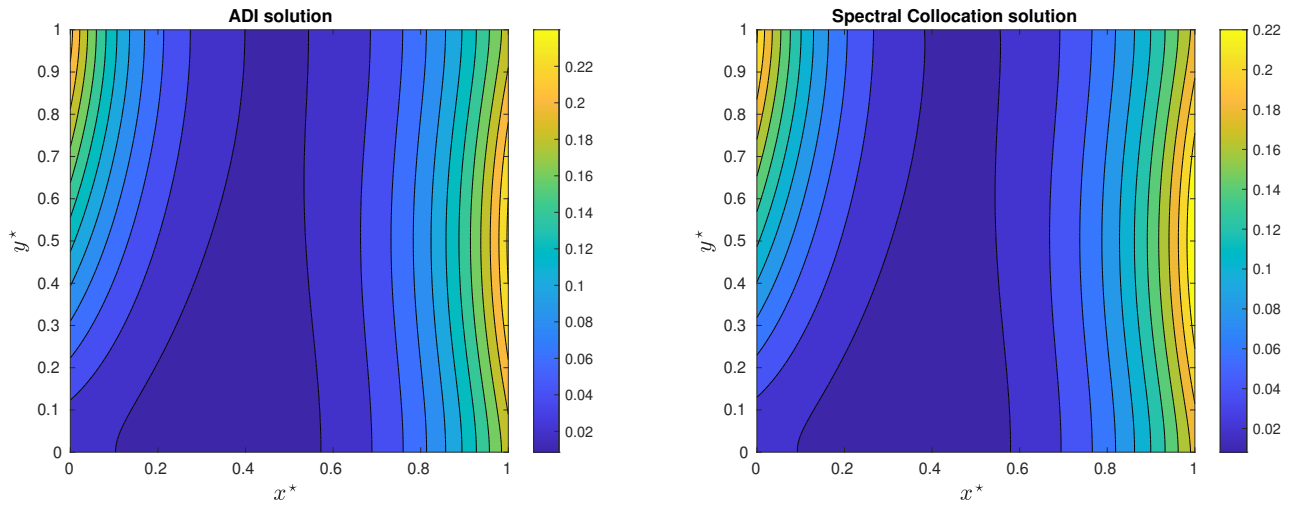


Figure 15. *Slices of the solution for the time instant $t^* = 6$.*

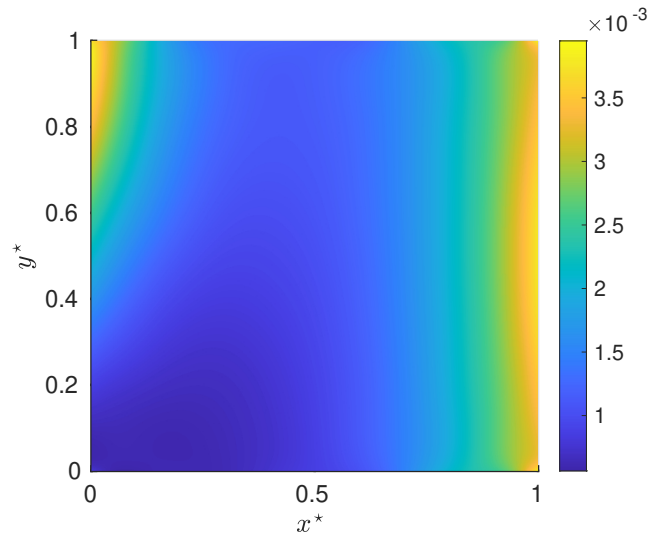


Figure 16. Error ε_2 as function of x^* and y^* axes.

Notes on contributors



Suelen Gasparin received her Ph.D. degree in Mechanical Engineer and Applied Mathematics from the Grenoble Alpes University, France and Pontifical Catholic University of Paraná, Brazil. After a postdoctoral fellow at the La Rochelle University, France, she is now a full researcher at the French Ministry of Environment, Cerema. She works on numerical methods for predicting heat and moisture transfer through porous building materials, based on advanced techniques such as Spectral model reduction approaches. Her objective is to develop fast and accurate models to represent the physical phenomena occurring in the porous building walls and their interactions with the ambient air.



Julien Berger received his PhD in 2014 from the Grenoble Alpes University, France. He is now a Tenured Associate Scientist at the French National Centre for Scientific Research. He contributes to the numerical methods applied for heat and moisture transfer in porous material. The proposed numerical model are based on innovative approach such as model reduction methods. They are employed for the computing the prediction of the physical phenomena for comparison with experimental observation to evaluate the overall model reliability. Models can also be employed in the framework of inverse problems to determine the diffusion material properties using *in-situ* measurement.



Giampaolo D'Alessandro received his M.S. and Ph.D. degree in Mechanical Engineering from University of L'Aquila, Italy, in 2014 and 2019, respectively. He has been a post-Doc student in the Department of Industrial and Information Engineering and Economics at University of L'Aquila, Italy, since 2019. His research activity is in the fields of heat conduction problems, parameter estimation and mass diffusion.



Filippo de Monte is a Professor of Mechanical Engineering at University of L'Aquila, Italy. He served as a full-time Visiting Ph.D. student at the Department of Engineering, University of Cambridge, UK, in 1992, and a seasonal Visiting Associate Professor at the Department of Mechanical Engineering, Michigan State University, USA, in 2007 up to 2014. He is a Member of American Society of Mechanical Engineers (ASME) and holds editorial positions at the Journal of Verification, Validation and Uncertainty Quantification (ASME) and Heat Transfer Engineering. He is co-editor of the Elsevier/Academic

Press 1st Edition book: Modeling of Mass Transport Processes in Biological Media (August 2022), and co-author of the Wiley 2nd Edition book: Inverse Heat Conduction: Ill-Posed Problems (Spring 2023), by Woodbury, Najafi, de Monte and Beck. His research interests include heat and mass transport by diffusion with applications to porous media, inverse heat transfer analysis, thermal properties estimation, refrigerating machines and Stirling thermal cycle. He is also ranked in the Top 2% of the world's scientists list compiled by Stanford University, 2020-2022.



Dariusz Ucinski was born in 1965. He received his MSc degree in electrical engineering from the Higher College of Engineering in Zielona Góra, Poland, in 1989, and his PhD and DSc degrees in automatic control and robotics from the Wrocław University of Science and Technology, Poland, in 1992 and 2000, respectively. In 2007 he was conferred the full professorial title, the highest scientific degree in Poland. He is currently a professor at the University of Zielona Góra, Poland. His research interests are in the area of measurement optimization for distributed parameter systems. He authored the book entitled Optimal Measurement Methods for Distributed Parameter System Identification (CRC Press, 2005). Other areas of his expertise include optimum experimental design, algorithmic optimal control, parallel computing, data analysis and machine learning.